Dynamical Role of Mode Water Ventilation in Decadal Variability in the Central Subtropical Gyre of the North Pacific*

SHANG-PING XIE

International Pacific Research Center and Department of Meteorology, University of Hawaii at Manoa, Honolulu, Hawaii, and Physical Oceanography Laboratory and Ocean–Atmosphere Interaction and Climate Laboratory, Ocean University of China, Qingdao, China

LIXIAO XU AND QINYU LIU

Physical Oceanography Laboratory and Ocean–Atmosphere Interaction and Climate Laboratory, Ocean University of China, Qingdao, China

FUMIAKI KOBASHI

Faculty of Marine Technology, Tokyo University of Marine Science and Technology, Tokyo, Japan

(Manuscript received 17 June 2010, in final form 12 September 2010)

ABSTRACT

Decadal variability in the interior subtropical North Pacific is examined in the Geophysical Fluid Dynamics Laboratory coupled model (CM2.1). Superimposed on a broad, classical subtropical gyre is a narrow jet called the subtropical countercurrent (STCC) that flows northeastward against the northeast trade winds. Consistent with observations, the STCC is anchored by mode water characterized by its low potential vorticity (PV). Mode water forms in the deep winter mixed layer of the Kuroshio–Oyashio Extension (KOE) east of Japan and flows southward riding on the subtropical gyre and preserving its low-PV characteristic. As a thick layer of uniform properties, the mode water forces the upper pycnocline to shoal, and the associated eastward shear results in the surface-intensified STCC.

On decadal time scales in the central subtropical gyre (15°–35°N, 170°E–130°W), the dominant mode of sea surface height variability is characterized by the strengthening and weakening of the STCC because of variations in mode water ventilation. The changes in mode water can be further traced upstream to variability in the mixed layer depth and subduction rate in the KOE region. Both the mean and anomalies of STCC induce significant sea surface temperature anomalies via thermal advection. Clear atmospheric response is seen in wind curls, with patterns suggestive of positive coupled feedback.

In oceanic and coupled models, northeast-slanted bands often appear in anomalies of temperature and circulation at and beneath the surface. The results of this study show that such slanted bands are characteristic of changes in mode water ventilation. Indeed, this natural mode of STCC variability is excited by global warming, resulting in banded structures in sea surface warming.

1. Introduction

Surface turbulent heat flux from the Pacific reaches a maximum along the Kuroshio and its extension in winter as the heat-carrying current meets cold and dry air advected from the Asian continent by the northeast monsoon. The deep mixed layer forms as a result, often exceeding 300 m in depth (Oka et al. 2011). With the

* International Pacific Research Center Publication Number 728 and School of Ocean and Earth Science and Technology Publication Number 8035.

Corresponding author address: Shang-Ping Xie, International Pacific Research Center, SOEST, University of Hawaii, Honolulu, HI 96822.
E-mail: xie@hawaii.edu

DOI: 10.1175/2010JCLI3896.1

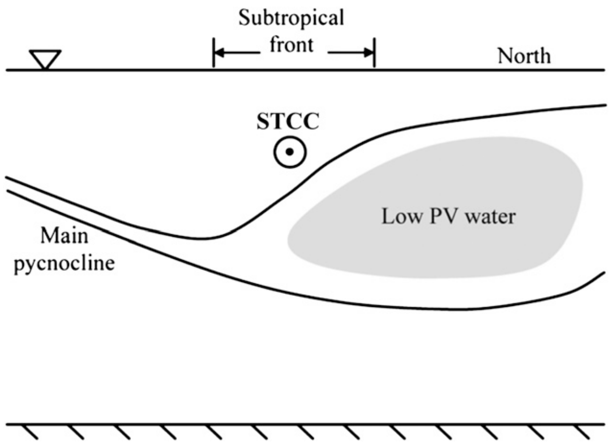

FIG. 1. Schematic of how mode water induces an eastward current above. With a gently sloping lower pycnocline, the upper pycnocline must shoal to accommodate the intrusion of a thick layer of mode water that circulates from the KOE region. The poleward shoaling of the upper pycnocline gives rise to the eastward STCC by thermal wind. From Kobashi et al. (2006).

mixed layer depth (MLD) shoaling rapidly southward, the southeastward geostrophic current subducts the mixed layer water into the thermocline, producing a thick layer of vertically uniform properties. Such mode water forms a vertical minimum in stratification within the otherwise strongly stratified thermocline. Once formed in the Kuroshio Extension, the mode water sweeps through the subtropical gyre, advected by the wind-driven gyre circulation (Hanawa and Talley 2001). Dynamically, mode water is characterized by a vertical minimum in potential vorticity (PV), which is approximated in the interior ocean as $q = f/h$, where f is the Coriolis parameter, and h is the thickness between neighboring isopycnal surfaces. Shielded from surface forcing, PV is considered to be conserved as mode water makes its way south, a principal assumption of the ventilated thermocline theory (Luyten et al. 1983; Kubokawa 1999).

Mode water is not simply a passive water mass. The fact that it carries distinct low-PV signals suggests potential dynamical effects on ocean circulation. Kubokawa (1999) shows that low-PV waters of different densities may overlap their paths on the horizontal plane as they circulate southward because of the beta spiral effect. They stack up in the vertical as a result, pushing the upper pycnocline upward (appendix). The poleward shoaling of the upper pycnocline anchors eastward vertical shear on the southern flank of the pile of mode water layers (Fig. 1). Using an ocean general circulation model (GCM), Kubokawa and Inui (1999) illustrate this mechanism for the formation of the subtropical countercurrent (STCC), an eastward-flowing current in the southern subtropical gyre where the Sverdrup theory predicts a broad westward flow (Uda and Hasunuma 1969; Yoshida and Kidokoro 1967). The hydrographic analysis of Kobashi et al. (2006) reveals a slanted STCC stretching from the western Pacific (20°N, 130°E) to the north of Hawaii (25°N, 160°W). Together with Aoki et al. (2002), Kobashi et al. show that the STCC is indeed anchored by mode waters beneath to the north. This result support Kubokawa's mode water ventilation mechanism for STCC. In fact, the northeastward tilt of the STCC axis is indicative of the effect of subtropical thermocline ventilation. Ocean eddy activity is locally enhanced along the STCC (Qiu 1999), with the presence of mode water increasing baroclinic instability (Liu and Li 2007). Vertical minimum in PV is observed to cluster into two distinct density modes at 25.5 and 26.2σ_θ, respectively called the subtropical and central mode waters (CMWs; Suga et al. 1997; Hanawa and Talley 2001). Both mode waters are important for the northeast-slanted STCC (Kobashi et al. 2006).

The STCC maintains a sea surface temperature (SST) front during winter and spring, called the subtropical front. During April and May when the SST front is still strong and the seasonal warming makes the region conducive to atmospheric convection, surface wind stress curls turn weakly positive along the front (Kobashi et al. 2008) on the background of negative curls that drive the subtropical gyre. On the weather time scale, positive wind curls are associated with low pressure systems of a subsynoptic scale in space, energized by surface baroclinity and latent heat release along the SST front. The SST front also anchors a meridional maximum in column-integrated water vapor, indicating a deep structure of the atmospheric response. Thus, mode water ventilation has a climatic effect in the interior subtropical gyre along the STCC.

The Kuroshio Extension displays large decadal variability (Miller et al. 1998; Deser et al. 1999; Qiu and Chen 2005; Nonaka et al. 2006), in response to wind shifts in the central and eastern North Pacific (Schneider and Miller 2001; Taguchi et al. 2007; Ceballos et al. 2009). Ocean GCM hindcasts forced by observed winds show significant variability in mode water ventilation in the central Pacific, which is accompanied by considerable anomalies of subsurface temperature (Xie et al. 2000; Hosoda et al. 2004). Indeed, Deser et al. (1996) have observed the subduction of temperature anomalies in the density range of 25–26σ_θ after the 1970s climate regime shift. Mode water variability could be due to changes either in ventilation path associated with circulation shifts (Yasuda and Hanawa 1997; Kubokawa and Xie 2002), subduction (Yamanaka et al. 2008; Qu and Chen 2009), or both (Ladd and Thompson 2002; Thompson and Dawe 2007). In an eddy-resolving ocean GCM, Yamanaka et al. (2008) show an interdecadal change in STCC; the countercurrent intensifies in the late 1970s with a strong southward intrusion of mode water and weakens in the early 1990s when the mode water ventilation is weak. They relate these decadal changes to variability in mode water formation and in basin-scale wind patterns.

Mode water has been hypothesized to affect SST upon obduction after circulating back to the Kuroshio and its extension (Hanawa and Talley 2001; Liu and Hu 2007). Recent studies reviewed above point to an additional dynamical role of mode water in climate by its effect on surface currents (e.g., STCC). Available hydrographic observations are inadequate to study variability in mode water ventilation—which is likely to be decadal or longer in time scale—and examine its effects on SST and the atmosphere. Long integrations of coupled GCMs are made available to the climate research community as part of the Intergovernmental Panel on Climate Change (IPCC) Fourth Assessment Report (AR4). If evaluated favorably in their skills in simulating mode water, these coupled integrations offer a useful tool to explore these issues.

The present study analyzes a multicentennial integration with the Geophysical Fluid Dynamics Laboratory (GFDL) coupled GCM to study processes by which mode water ventilation affects surface currents, SST, and the atmosphere over the North Pacific. We wish to address the following questions: how well does the model simulate the formation and circulation of mode water? Does the model form the STCC, and what role does mode water play? Is mode water a major factor in decadal variability? If so, does the mode water variability induce significant SST anomalies? Can we detect an atmospheric signal and is there feedback between the ocean and atmosphere? We show that the GFDL model captures the dynamical role of mode water in STCC formation and variability. In the model, there is a distinct mode of interdecadal variability in which mode water plays a central role by modulating STCC. There is evidence for a positive ocean–atmosphere feedback in this low-frequency mode triggered by mode water variability. This mode of variability is not unique to the GFDL model but has been seen in the National Center for Atmospheric Research (NCAR) Community Climate System Model version 3 (CCSM3), and other state-of-the-art coupled GCMs (not shown). In coupled model simulations with or without changes in climate forcing, banded structures with a northeast slant often appear in SST or subsurface temperature anomalies in the subtropical gyre. For example, Xie et al. (2010) note such slanted bands in SST warming in a GFDL model projection under the A1B scenario. We will show that such northeast-slanted structures are characteristic of anomaly patterns created by changes in mode water ventilation.

The rest of the paper is organized as follows. Section 2 briefly describes the model and analysis methods. Section 3 evaluates the simulated climatology and compares with observations where appropriate. Section 4 investigates interdecadal variability in the interior subtropical gyre of the North Pacific and how mode water ventilation is a key process for this variability. Section 5 examines the SST and atmospheric signatures of this mode and discusses implications for global warming simulations. Section 6 is a summary.

2. Model and methods

We analyze a 300-yr control simulation by the National Oceanic and Atmospheric Administration (NOAA) GFDL climate model (CM2.1). Under the climate forcing consistent with the year of 1860, the coupled model is integrated for 220 yr as spinup. The 300-yr control run we analyze (CM2.1U_Control-1860_D4) follows this spinup period. The CM2.1 uses the Flexible Modeling System (FMS) to couple the GFDL atmospheric model (AM2.1) with the Modular Ocean Model version 4 (MOM4). The AM2.1 builds on a finite volume atmospheric dynamical core and includes atmospheric physical packages and a land surface model. Its resolution is 2° latitude × 2.5° longitude with 24 vertical levels, nine of which are located in the lowest 1.5 km to represent the planetary boundary layer. The ocean model uses a finite difference approach to solve the primitive equations. The resolution is 1° latitude by 1° longitude, with meridional grid spacing decreasing to 1/3° toward the equator. The model has 50 vertical levels, 22 of which are in the upper 220 m. A detailed description of CM2.1 can be found in GFDL Global Atmospheric Model Development Team (2004) and Delworth et al. (2006).

The IPCC Special Report on Emissions Scenarios (SRES) A1B scenario for the emission of a few climatically important trace gases is based on certain socioeconomic development paths for the twenty-first century. It projects a rough doubling of atmospheric CO_2 for the century. A 10-member ensemble simulation has been made with CM2.1 for the A1B scenario up to 2050 (Xie et al. 2010). Ensemble-mean, 50-yr difference fields are formed for the A1B simulations from 1996–2000 to 2046–50.

CM2.1 features energetic El Niño–Southern Oscillation (ENSO; Wittenberg et al. 2006). In analyzing the control run, we apply a 9-yr low-pass filter to remove ENSO and other interannual variability. We have performed an empirical orthogonal function (EOF) analysis for sea surface height (SSH) over the central subtropical gyre. The unfiltered leading principal component (PC) displays two peaks in spectrum, at 5 and 40 yr with a trough at 9 yr.

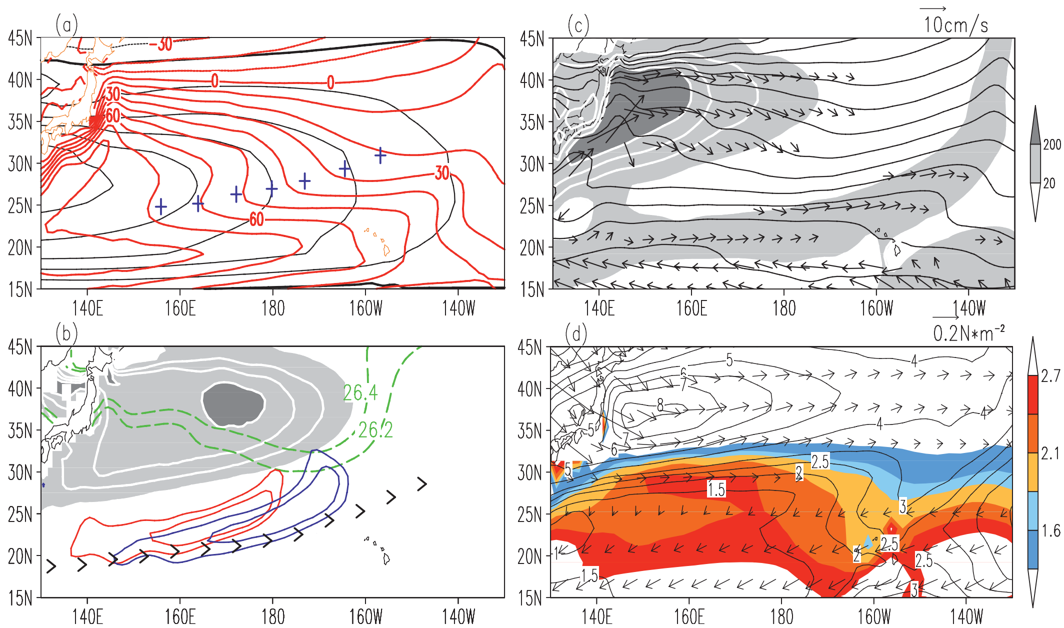

FIG. 2. March climatology. (a) Annual-mean Sverdrup streamfunction [black contours at 20-Sv (1 Sv $\equiv 10^6$ m^3 s^{-1}) intervals], SSH (red contours at 10-cm intervals), and plus symbols denote where a PV minimum is reached in the layer of 26.0–26.6σ_θ. (b) PV on 26.2 (red contours at 0.8 and 1.0 $\times$ 10^{-10} m^{-1} s^{-1}) and 26.4 (blue contours) isopycnals, along with the mixed layer depth (light/dark shade > 100/400 m; white contours at 100-m intervals), surface density (green), and ">" symbols denote the axis of STCC. (c) 50-m current velocity, SST (black contours at 2°C intervals), and net surface heat flux (gray shade; white contours at 60 W m^{-2} intervals). (d) Surface wind stress (N m^{-2}), Ekman pumping velocity (color shade at 1.0 $\times$ 10^{-6} m s^{-1} intervals), and precipitation (black contours at 0.5 kg m^{-2} s^{-1}).

Lee (2009) has examined changes in the North Pacific subtropical mode water (STMW) in response to global warming in the same model. He finds that STMW temperature is correlated with both the Kuroshio heat transport and winter monsoon intensity. He does not study the dynamical consequence of mode water change, a topic that is the focus of our study.

3. Mean state

This section examines the climatology defined as the average from year 1 to 300. Figure 2a shows the annual-mean SSH field. The model simulates a basin-scale anticyclonic subtropical gyre circulation. An eastward jet is embedded in the central gyre (20°–30°N) where the Sverdrup zonal flow is sluggish. Flowing against the northeast trade winds, this STCC originates in the western Pacific around 20°N, intensifies into a speed exceeding 10 cm s^{-1} near the international date line, and then merges with the broad eastward flow northeast of Hawaii.

As in observations (Aoki et al. 2002; Kobashi et al. 2006), the model STCC is anchored by low-PV water to the north. Figure 3 shows zonal current and PV in a latitude–depth section along the international date line. The STCC is a surface eastward current confined to the upper 200 m, in thermal wind balance with the northward shoaling of the upper pycnocline ($\sigma_\theta < 26.25\sigma_\theta$ at this longitude). In 20°–25°N where the STCC is found, the lower pycnocline (e.g., 27σ_θ) slopes downward as predicted by the Sverdrup theory. The 26.5σ_θ isopycnal begins to shoal northward as a thick layer of low-PV water is found underneath. The 26.25σ_θ isopycnal shows an even steeper northward shoaling, pushed by low-PV water in the 26.25–26.5σ_θ layer (25°N). Thus, the STCC is closely associated with mode water underneath, which is in turn determined by upstream conditions in the ventilated thermocline. This is consistent with Kobashi et al. (2006) who relate the eastward shear to negative PV gradients in the underneath mode water layer. Indeed in the model, the PV minimum (marked by plus symbols) in a broad density range of 26–26.6σ_θ is found consistently north of the STCC (Fig. 2a), following a similar slanted track. The appendix discusses the baroclinic adjustment to an intrusion of mode water, explaining both the STCC and the intensification of the westward flow underneath.

In the Northwest Pacific, intense surface cooling creates a deep mixed layer in winter along the Kuroshio–Oyashio Extension (KOE). A sharp MLD front forms between the deep mixed layer in KOE and the shallow

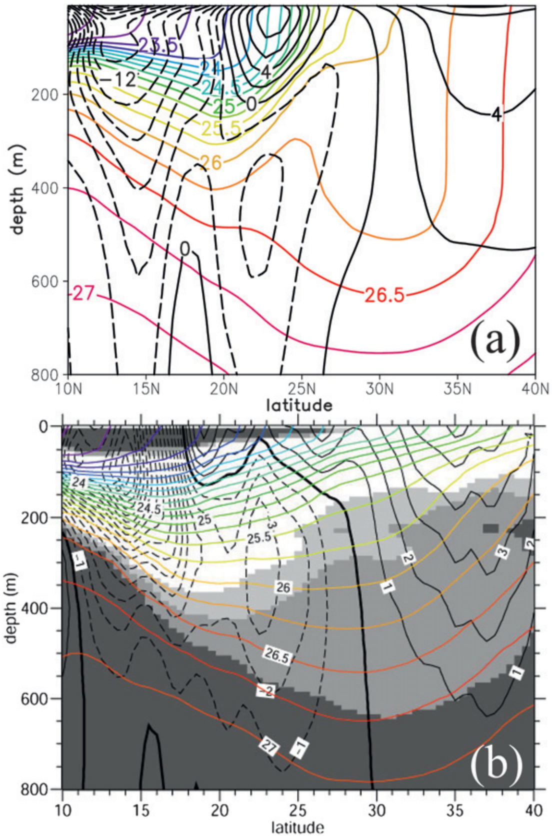

FIG. 3. (a) March potential density (color contours) and zonal velocity (black contours at 2 cm s^{-1} intervals) at 180° as a function of latitude and depth in CM2.1. (b) Observed annual-mean climatology of potential density (color contours), zonal geostrophic velocity (cm s^{-1}) relative to 1000 dbar, and PV (gray shade at 0.5×10^{-10} m^{-1} s^{-1}) at 180°.

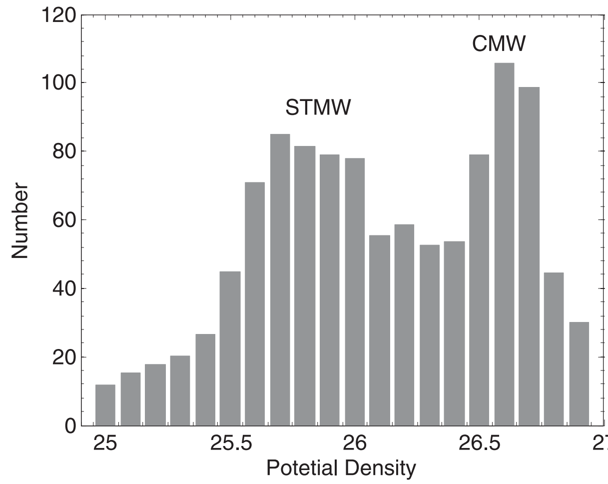

FIG. 4. Number of grid points over the North Pacific with a vertical PV minima of less than 1.5×10^{-10} m^{-1} s^{-1}.

one to the south and east (Fig. 2b). Mode water forms at the cross point between the MLD front and the outcrop line (surface density isoline), where the vertically uniform water in the deep mixed layer is subducted into the main thermocline (Kubokawa 1999; Xie et al. 2000). Following Williams (1991), potential vorticity at the point of subduction may be expressed as

$$q_m = \frac{f}{\bar{\rho}} \cdot \frac{\mathbf{u}_m \cdot \nabla \rho_m}{\mathbf{u}_m \cdot \nabla z_m + w_e}, \tag{1}$$

where w_e is Ekman pumping velocity, $\mathbf{u}_m \cdot \nabla z_m$ represents lateral induction of the deep mixed layer water into the thermocline across the MLD front, ρ is density, z_m is MLD, and $\mathbf{u}_m$ is the current velocity in the mixed layer. Along the MLD front, the lateral induction dominates (Huang and Qiu 1994; Qu et al. 2002). In the model, low-PV waters indeed form at the intersection of the MLD front and outcrop line (Fig. 2b), where the lateral induction term in the denominator of (1) reaches the maximum for a given density. After subduction, they flow southward following the subtropical gyre and form a tongue of PV minimum on each isopycnal surface. Because of the beta spiral effect, PV minima on different isopycnals ($26.2\sigma_\theta$ and $26.4\sigma_\theta$ in Fig. 2b), while subducted in different places, can have their paths overlap as they flow southward, creating a thick layer of small PV over a broad range of density in support of STCC formation as Fig. 3 depicts at 180°.

a. Comparison with observations

Figure 4 shows the number of grid points with a vertical PV minimum as a function of the density where the PV minimum appears. A PV minimum tends to occur in two distinct density ranges: 25.6–$26.0\sigma_\theta$ and 26.5–$26.7\sigma_\theta$. The bimodal distribution is similar to observations (Fig. 10 of Kobashi et al. 2006) but the model mode waters are too dense by $0.3\sigma_\theta$. In observations, PV minima are clustered in 25.3–$25.7\sigma_\theta$, and 26.1–$26.5\sigma_\theta$, making the STMW and the CMW, respectively (Suga et al. 1989, 1997; Nakamura 1996; Hanawa and Talley 2001). The $0.3\sigma_\theta$ dense bias in mode water core is consistent with too large surface density in KOE. At the international date line, where the CMW forms, the $26.0\sigma_\theta$ outcrop line is located at 38°N in observations but south of 30°N in the model (Fig. 5a versus Fig. 2a).

On an isopycnal, the low-PV tongue is much more diffused in observations than in the model, with a broader spatial structure and larger PV values (Fig. 5b). The PV minimum in mode water is typically 1.5×10^{-10} m^{-1} s^{-1} in the observed climatology, whereas it can be as low as 0.5×10^{-10} m^{-1} s^{-1} in the model. In the observed meridional transect (Fig. 3b), the STCC at 26.5°N is anchored by PV minima on isopycnals of 25.5–$26.5\sigma_\theta$ to the north, but these

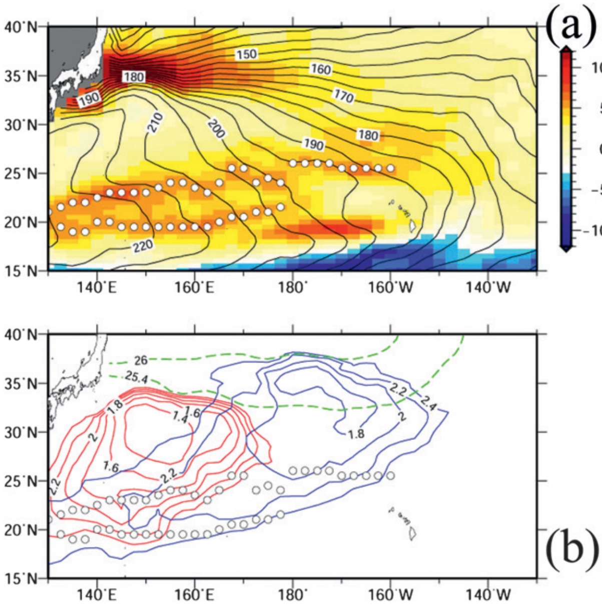

FIG. 5. Observed annual-mean climatology. (a) Surface geostrophic velocity relative to 400 dbar (color in cm s^{-1}) and sea surface dynamic height referenced to 1000 dbar (contours in cm). (b) Winter sea surface density (green contours) and PV (contours at 0.2×10^{-10} m^{-1} s^{-1} intervals for values less than 2.4×10^{-10} m^{-1} s^{-1}) on 25.4 (red) and 26.0 (blue) isopycnals, representative of the STMW and CMW. Open circles denote the position of the STCC.

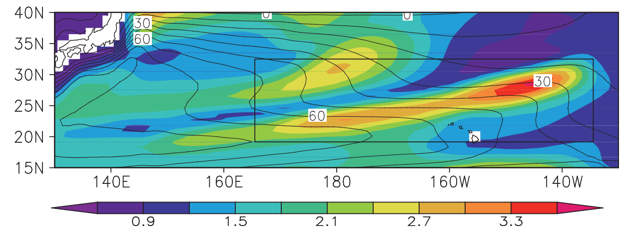

FIG. 6. Standard deviation of decadal variability in SSH (shaded at cm), superimposed on the annual-mean SSH (contours at 10 cm intervals). The box denotes the central gyre domain for the EOF analysis in Fig. 7.

PV minima are not as pronounced as in the model, say on 26.25–26.5σ_θ isopycnals. [The eastward surface velocity at 19°N is associated with the Hawaiian Lee Countercurrent (Fig. 5a) induced by the orographic wind effect of Hawaii (Xie et al. 2001).]

Kobashi et al. (2006) show that the western STCC actually splits into two distinct jets in observations (Fig. 5a), a structure the model does not capture. In the model, the western STCC jet continues along a northeast-slanted path, confirming what Kobashi et al. call the eastern STCC observed north of Hawaii. The eastern STCC is too strong in the model compared to observations, a bias likely due to too strong mode waters. This bias is associated with too strong a northward shoaling of the upper thermocline, manifested as a northeast-slanted band of cold errors in the top 200-m temperature as noted by Gnanadesikan et al. (2006, their Fig. 12b).

Noneddy-resolving models tend to produce too strong mode waters (Ladd and Thompson 2001). Eddy-resolving models seem to improve mode water simulation with more realistic, diffused PV-minimum structures (Yamanaka et al. 2008; H. Sasaki et al. 2010). We note, however, a strong eastern STCC still appears in an eddy-resolving ocean GCM with realistic wind and buoyancy forcing (Yamanaka et al. 2008).

b. Atmospheric effect

The STCC leaves visible signatures in surface climate. In the March climatology, net surface heat flux out of the ocean reaches a local maximum along the countercurrent because of its distinct northeastward warm advection on the background of southward Sverdrup flow in the subtropical gyre (Fig. 2c). This warm advection is also manifested in a ridge of SST contours along the STCC, a feature especially clear north of Hawaii. Along this SST ridge, precipitation displays a weak but visible local maximum and so does the Ekman pumping velocity (Fig. 2d). This Ekman pumping velocity signature of STCC is similar to Kobashi et al. (2008) except that in their Quick Scatterometer (QuikSCAT) observations, this atmospheric effect is most pronounced in the western STCC. This is because the STCC is stronger in the east than west in the model while the reverse is true in observations. Tokinaga et al. (2009) note similar climatic effects of the eastern STCC in CCSM3.

Thus, CM simulates the formation and ventilation of mode waters and their dynamical effect on surface current in the form of STCC, broadly consistent with the

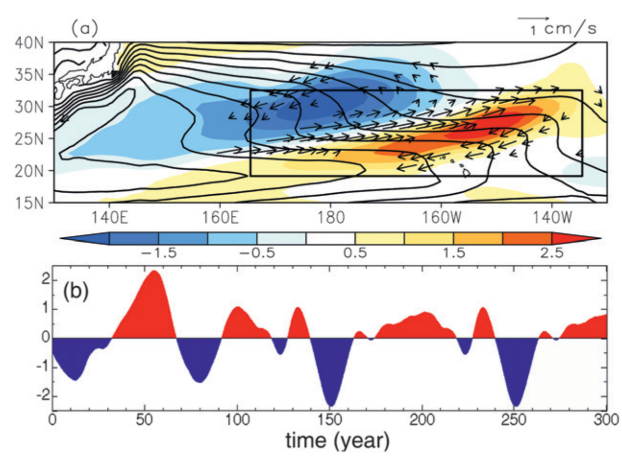

FIG. 7. (a) First EOF mode for SSH (color shade in cm) in the central gyre region (box) and (b) its principal component. Mean SSH (black contours at 10 cm intervals) and regression of 50-m current velocity upon the PC are superimposed in (a).

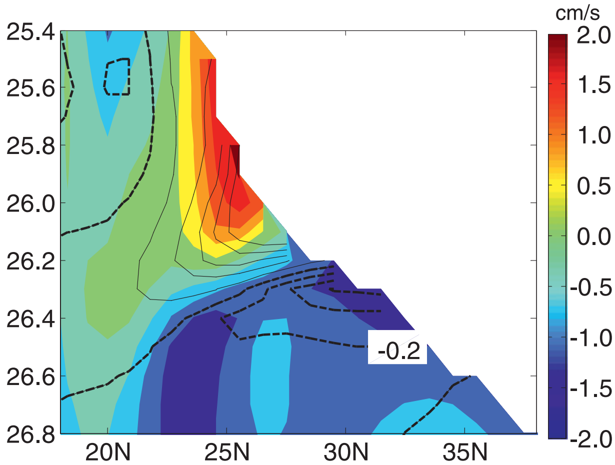

FIG. 8. Regression of PV (black contours at 0.2×10^{-10} m^{-1} s^{-1} intervals) and zonal velocity (color shade) upon the SSH PC-1 as a function of latitude and potential density along 180°. Low-PV anomalies in 26.2–26.6σ_θ anchor the intensified STCC to the south near the surface.

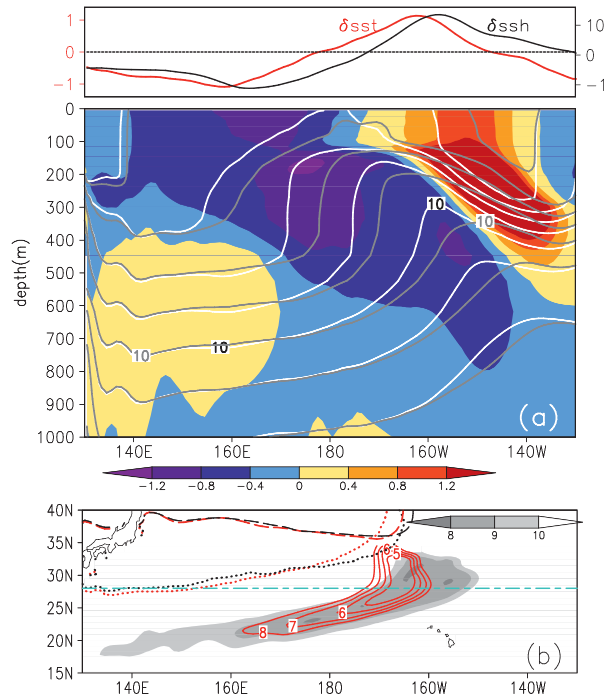

FIG. 9. (a) Temperature at the high (white contours) and low (gray) phases of SSH PC at 28°N, along with their difference (color shade). (top) Corresponding SSH and SST differences are shown. (b) PV (in 1.0×10^{-11} m^{-1} s^{-1}) on the 26.5σ_θ surface at the high (red contours) and low (gray shade) phases of SSH PC. The 100-m MLD contour (dotted) and outcrop line (dashed) are also plotted.

observations of Kobashi et al. (2006). The model also simulates an atmospheric response to the thermal effect of the STCC, in qualitative agreement with observations. We note that the model displays biases, notably a too strong eastern STCC. The agreement with observations is encouraging enough that we will proceed to examine decadal variability in the model.

4. STCC mode of interdecadal variability

Figure 6 shows the standard deviation of SSH variability on decadal and longer time scales. (Of much stronger variability, the KOE region is excluded in the plot for clarity.) In the interior subtropical gyre away from KOE, a pair of high-variance bands is striking, both slanted and each collocated with a ridge in mean SSH. [The zonal band to the south at 10°–15°N is likely associated with variability in the intertropical convergence zone (Capotondi et al. 2003).] The long slanted band roughly coincides with the STCC ridge, stretching from the western Pacific through north of Hawaii.

We perform an EOF analysis for SSH in a central subtropical gyre domain (18.5°–32.5°N, 165°E–135°W) that the STCC high-variance band transverses. Figure 7 shows the pattern and PC of the leading mode, which explains 43.2% of the total variance in the central gyre domain (box in the figure). SSH anomalies in the STCC band turn out to be opposite in phase with those in the high-variance band to the northwest. The northeast-slanted dipole pattern is such that the STCC strengthens and displaces northward at the positive phase. The PC is of interdecadal time scales, with a typical time scale of 50 yr. Hereafter, we call the interdecadal variability the STCC mode. The rest of this section shows that the STCC mode originates from the KOE.

a. *Mode water variations*

The STCC mode is associated with large changes in mode water ventilation. Figure 8 shows regressions of PV and zonal velocity upon the SSH PC-1 at 180°. The strengthening of the eastward STCC is associated with negative PV anomalies underneath to the north, in a layer of 26.2–26.6σ_θ. (These current and PV anomalies discussed here are significant with correlation exceeding 0.5.) This is consistent with the mode water mechanism for eastward surface current (Kubokawa 1999; Kobashi et al. 2006).

Figure 9a compares ocean temperature at 28°N at the high and low phases of the STCC mode. The high (low) phase is defined as when SSH anomalies are positive (negative) along the climatological STCC (Fig. 7a). Mode waters characterized by large layer thickness are obvious at both phases. At the high phase on a given isotherm (white contours), the PV minimum is visibly lower in magnitude (corresponding to larger layer thickness) and shifted to the west in location. As a result, isotherms are pushed upward along the down-eastward-slanted band of

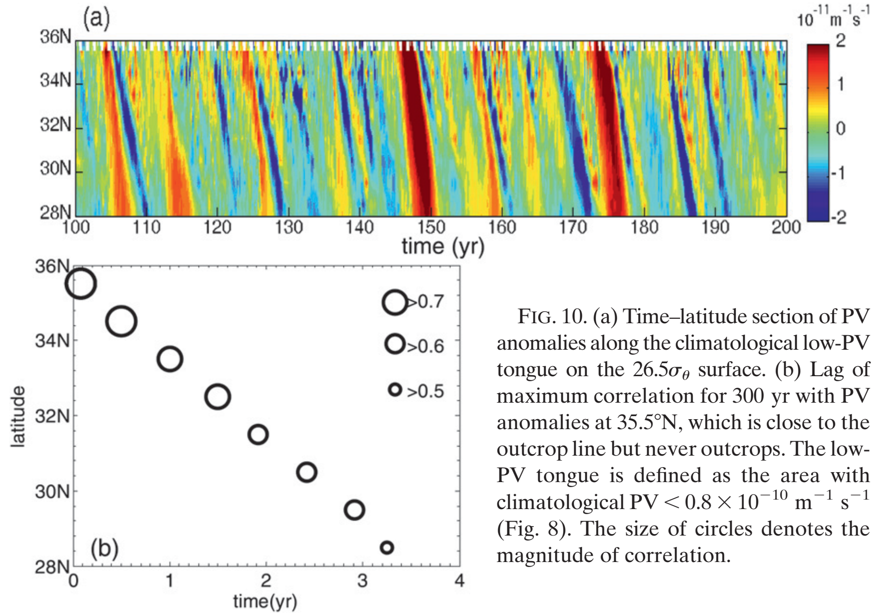

FIG. 10. (a) Time–latitude section of PV anomalies along the climatological low-PV tongue on the $26.5\sigma_\theta$ surface. (b) Lag of maximum correlation for 300 yr with PV anomalies at 35.5°N, which is close to the outcrop line but never outcrops. The low-PV tongue is defined as the area with climatological PV $< 0.8 \times 10^{-10}$ m^{-1} s^{-1} (Fig. 8). The size of circles denotes the magnitude of correlation.

low PV, lowering SSH west of 170°W. To the east, by contrast, the westward shift of mode waters allows isotherms to sink, giving rise to temperature warming and positive SSH anomalies. The weakening of mode waters at the low phase also contributes to the subsurface warming in a down-eastward-slanted region. Figure 9b compares low-PV tongues on the $26.5\sigma_\theta$ surface between the high and low phases of the STCC mode, showing the westward displacement and the deepened PV minimum at the high phase.

Isopycnal PV anomalies can be traced back upstream to the formation region of low-PV water. Figure 10 shows PV anomalies on the $26.5\sigma_\theta$ surface along the low-PV tongue in a distance–time section. The along-trajectory propagation is obvious. This along-path phase propagation is quantified by the lagged correlation with the PV anomalies at 35.5°N, where the $26.5\sigma_\theta$ surface is close to the outcrop line but never outcrops. For a PV anomaly formed at 35.5°N, it takes 2 yr for it to reach 31°N where the PV tongue takes a southwest turn and another year to reach 28.5°N.

b. Subduction variations

Since PV anomalies can be traced back to the subduction region on a given isopycnal, this subsection investigates the cause of original PV anomalies at subduction. Figure 11 shows anomalies of surface wind, MLD, subduction rate calculated from Eq. (1), and current velocity in March three years before the STCC mode peaks. The mixed layer shallows on the southeast edge of the deep MLD region while deepening by as much as 100 m inside the deep MLD region to the west. This MLD dipole represents

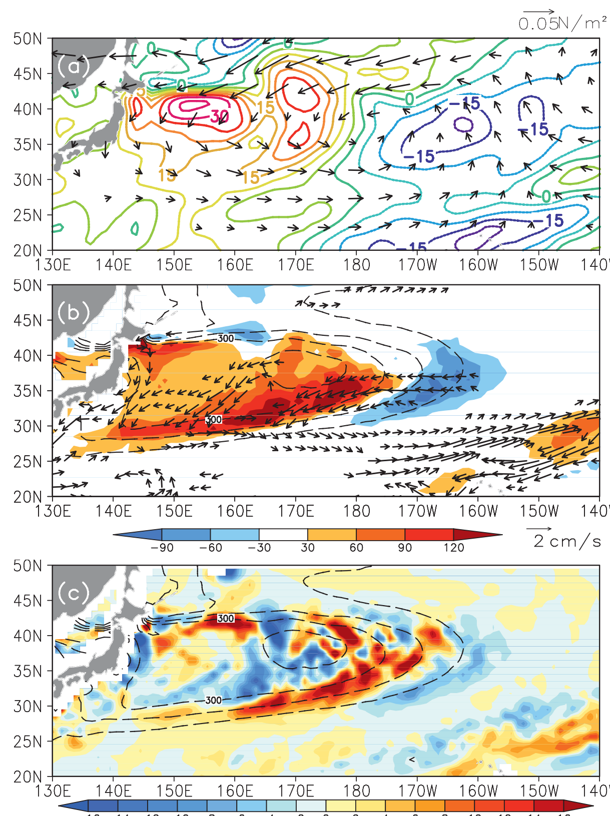

FIG. 11. Anomalies in March 3 yr prior to the peak of SSH PC based on linear regression: (a) surface wind stress (N m^{-2}) and net surface heat flux (W m^{-2}); (b) surface current velocity (cm s^{-1}), MLD (color shade in m), and mean MLD (black contours); and (c) lateral induction (1.0×10^{-6} m s^{-1}) and mean MLD (black contours).

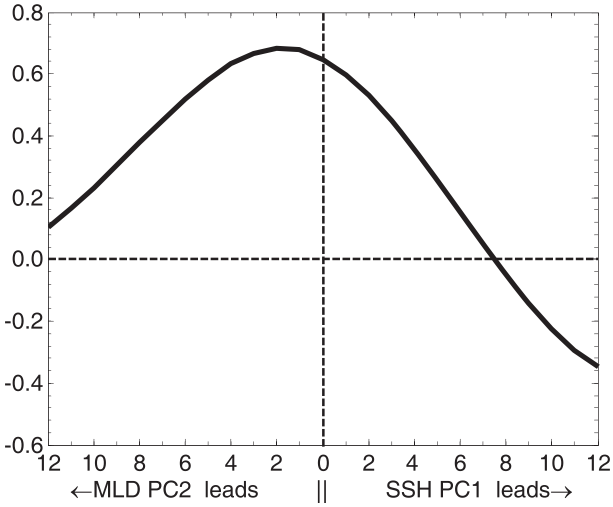

FIG. 12. Lead-lag correlation of the MLD PC-2 with the central gyre SSH PC-1. The MLD EOF analysis is for March and over a KOE domain of 25°–40°N, 140°E–150°W.

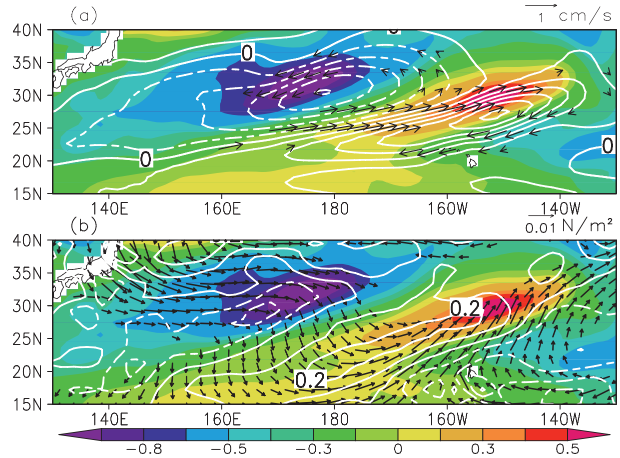

FIG. 13. March anomalies based on regression upon the SSH PC-1: SST (shaded in °C) along with (a) SSH (white contours at 1 cm) and 50-m current velocity (cm s^{-1}); (b) surface wind stress (N m^{-2}) and Ekman pumping velocity (white contours at 0.1×10^{-6} m s^{-1}).

a slight westward retreat of the MLD front and a sharp increase in MLD gradient. Wind anomalies are characterized by a basin-scale cyclonic circulation centered at 37°N, 175°W. The deepened MLD appears owing to the intensified surface heat loss associated with cold advection by the anomalous northerly wind, consistent with Qu and Chen's (2009) analysis of an eddy-resolving ocean GCM hindcast. Because of the large SST gradient in the mean in KOE, surface heat flux variability appears to be more correlated with meridional than zonal wind anomalies.

In the KOE region, subduction rate controls PV values at the time of subduction, both dominated by the lateral induction effect along the MLD front. We have calculated subduction rate change at the 3-yr lead based on Eq. (1). The sharpening of the MLD front increases the subduction rate (Fig. 11c) and lowers the PV values of mode waters at their formation. (The anomalous current effect on subduction rate is significantly smaller in magnitude and modifies slightly the subduction rate anomaly patterns.)

Thus, basin-scale wind variability modulates the sharpness of the MLD front of KOE. The resultant change in subduction rate induces PV anomalies at the time of mode water formation. These PV anomalies are advected into the interior subtropical gyre, giving rise to variability in the STCC. We have computed the subducton rate integrated in the mode water formation region (bounded by MLD = 200–300 m and 26–26.6σ_θ). Indeed, this subduction index is correlated with the SSH PC-1 at $r = 0.51$, at 3-yr lead. We have also conducted an EOF analysis of March MLD variability in the KOE region of 25°–40°N, 140°E–180°. Explaining 20% of variance, the second EOF resembles the dipole pattern of MLD anomalies along KOE pattern in Fig. 11b. Its PC correlation with the STCC mode peaks at $r = 0.68$ when leading by 2 yr (Fig. 12), in support of the notion that MLD and subduction rate changes are the major cause of downstream variability in STCC.

Following Taguchi et al. (2007), we have performed an EOF analysis of KOE SSH averaged zonally in 145°E–180°. The second mode explains 26% of the total variance within 30°–45°N and represents a weakened KOE current (not shown). The KOE PC-2 correlates with the STCC PC-1 at $r = 0.76$ with a 5-yr lead, an association seen in Fig. 11b. The relationship among wind, KOE, MLD, and subduction needs further investigations.

5. Climatic effects

a. SST and atmospheric response

In the March climatology, the northeastward STCC creates an SST ridge and imprints on surface heat flux, precipitation, and wind stress curl (Fig. 2). With strong SST gradients in the winter and spring climatology, it is conceivable that interdecadal variability in STCC is likely to affect SST and the atmosphere. Figure 13a superimposes the SSH EOF and the SST regression upon the SSH PC in March. SST anomalies are nearly 90° out of phase with SSH, positive with northeastward current anomalies. This phase relation suggests the importance of advection of mean SST gradient by anomalous currents.

The slanted band of positive SST anomalies induces southwesterly wind anomalies on its south flank, accompanied by positive wind curl anomalies (Fig. 13b).

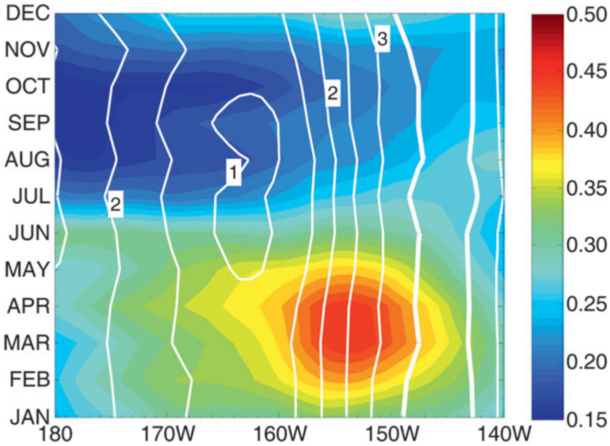

FIG. 14. Standard deviations of SSH (contours at 0.5-cm intervals) and SST (color shade in °C) variability at 28°N as a function of longitude and calendar month.

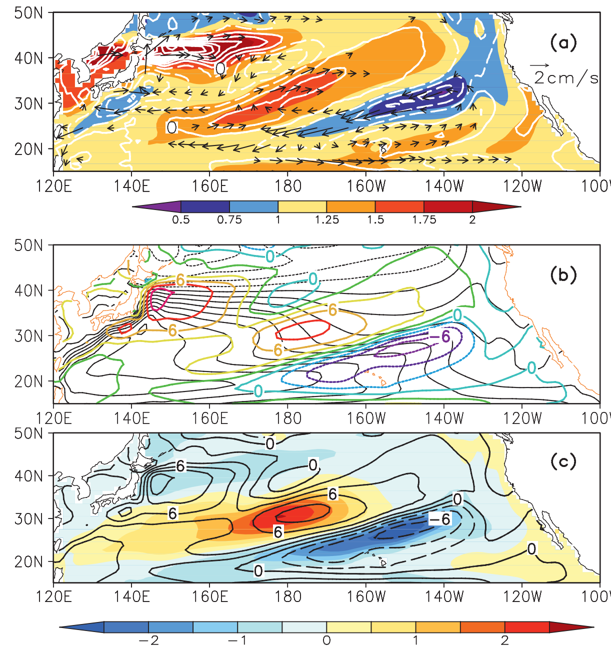

FIG. 15. 50-yr (2000–2050) changes in March in the A1B global warming simulation: (a) SST (°C), 50-m current velocity (cm s^{-1}) and net surface heat flux (white contours at 5 W m^{-2}); SSH change (contours in cm) superimposed on (b) the climatology (black contours), and (c) the SSH EOF mode 1 over the central subtropical gyre (color shade).

Similarly to the west, negative wind curl anomalies are nearly collocated with the negative pole of the SST dipole pattern. The Ekman pumping response appears to provide positive feedback onto SST as follows. Positive Ekman pumping forces a northward Sverdrup flow that acts to strengthen the SST warming, and the SST warming is what gives rise to the positive Ekman pumping anomaly in the first place. This feedback mechanism via Sverdrup flow advection is first proposed by Liu (1993) in a theoretical study that explores how ocean mixed layer processes affect ocean–atmosphere interaction in the midlatitudes. In coupled GCMs like CM, this feedback mechanism is triggered by variability in mode water ventilation and amplifies anomalies of SST, Ekman pumping, and ocean thermal advection by their mutual interaction.

Because of the slow time scale of the propagation of mode water anomalies via ventilation, interdecadal SSH variability displays little seasonality (Fig. 14), with amplitude of 3.5 cm. The SST variance, by contrast, experiences large seasonal variations, reaching a maximum in March–April of 0.5°C in standard deviation. This seasonality of SST variability is due to the seasonal cycle in SST climatology, which features the lowest temperature and sharpest gradient in March. At 28°N, the SST variance maximum is displaced on the west flank of the SSH variance maximum, suggestive of the importance of meridional thermal advection for SST variability.

b. *Implications for global warming*

In an analysis of the CM future climate projection under the A1B scenario of atmospheric trace composition change, Xie et al. (2010) note banded structures in SST warming over both the subtropical North Pacific and Atlantic. These bands slant in a northeast direction, which Xie et al. suggest is indicative of changes in mode water ventilation. Figure 15a shows these slanted banded structures in SST and 50-m current changes for 50 yr from 1996–2000 to 2046–50, averaged with 10-member ensemble integrations of CM2.1. Patterns of SST warming north of 20°N are associated with ocean current changes. The central subtropical gyre is marked by a northeast-slanted dipole of SST warming. The enhanced and reduced warming in the east and west, respectively, are associated with the northeastward and southwestward current anomalies that advect the mean poleward SST gradient. Indeed, net surface heat flux anomalies are upward over the warm SST path and vice versa. As in natural variability, the banded structures in SST warming are most pronounced in winter and spring (not shown) when the mean SST gradient is strong.

Current anomalies are in geostrophic balance with SSH change. By superimposing the mean SSH, it is clear that the SSH change represents a weakening of the STCC (Fig. 15b); a band of negative SSH anomalies is collocated with the mean SSH ridge that gives rise to the STCC in climatology. In-depth analysis confirms that the mode water ventilation weakens in global warming as the winter mixed layer shoals in the KOE region (F. Kobashi 2009, personal communication; Luo et al. 2009), resulting in a reduced subduction and weakened STCC downstream.

Figure 15c compares the natural STCC mode at the negative phase and SSH change in response to global warming. Over the central subtropical gyre (15–35°N, 170°E–130°W), their similarity is striking, both featuring a northeast-slanted dipole. This resemblance indicates that the STCC mode is excited in global warming by subduction changes in the mode water formation region along KOE. The dipole of SSH change in global warming is very large compared to the interdecadal STCC mode, 6–8 cm as opposed to 3 cm in amplitude.

6. Summary and discussion

We have investigated mode water ventilation, its role in STCC formation, and their covariability over the North Pacific using the GFDL CM. Superimposed on the spatially smooth, basin-wide subtropical gyre is a narrow northeastward jet slanted in a northeast direction. The northeast slant of this jet results from mode water ventilation in the subtropical thermocline. Mode water forms in the deep winter mixed layer along the KOE and circulates in the subtropical gyre preserving its low-PV characteristic. The beta spiral effect steers the paths of mode waters of different density to overlap on the horizontal plane, stacking them up in the vertical and creating a thick layer of relatively uniform water. To accommodate this thick layer of water, the upper pycnocline shoals. The resultant poleward shoaling of the upper pycnocline supports the eastward STCC by thermal wind. The association between the STCC and mode water underneath is consistent with the theory of Kubokawa (1999) and hydrographic observations of Kobashi et al. (2006). Our model results confirm Kobashi et al.'s observations that the eastern STCC is anchored by the central mode water and suggests that it is connected with the western STCC.

Basin-wide wind variability induces anomalies in KOE MLD and subduction change across the MLD front. An increase in subduction in response to the sharpened MLD front lowers the PV of subducted mode water. This PV anomaly is advected southeast then southwestward to the north of the STCC, causing the upper pycnocline to shoal more than normal and intensifying the STCC. On decadal time scales, this variability in STCC turns out to be the dominant mode of SSH in the interior/central subtropical gyre. At the negative phase of this STCC mode, the central mode weakens and its path shifts anomalously eastward.

The northeastward STCC causes a local enhancement of precipitation and a local minimum in Ekman downwelling, confirming Kobashi et al.'s (2008) satellite observations (which show stronger atmospheric response in the western STCC, though). The STCC mode of interdecadal variability is associated with considerable SST anomalies due to advection of mean SST gradient by anomalous currents. Indeed, SST variability is most pronounced during March–April when the mean SST gradient is strong, despite little seasonality in SSH anomalies. Significant atmospheric response is found in surface wind and Ekman pumping fields, suggestive of a positive feedback with SST via thermal advection by anomalous Sverdrup flow as proposed by Liu (1993) in a theoretical study. Thus, our study points to a new dynamical mechanism for mode water to affect climate, by its effect on surface current (STCC) and thermal advection. This mechanism takes place along the STCC where mode waters of different density overlap in vertical stack. This contrasts to the traditional view—a variant of reemergence mechanism (Alexander et al. 1999; Sugimoto and Hanawa 2005)—that mode waters release their anomalies of temperature and other properties when circulating back to the deep MLD region of KOE (Hanawa and Talley 2001).

In response to increased greenhouse gas concentrations in the atmosphere, the surface ocean warming is highly uneven in spatial distribution (Xie et al. 2010). We show that the STCC mode of natural circulation variability is selectively excited in the global warming simulation with the same model. In a warmer climate, the STCC weakens, leaving behind banded structures in SST warming with the characteristic northeast slant. The STCC mode is among the few natural modes that are excited by global warming and imprint on SST patterns. The Indian Ocean dipole is another, with a reduced warming and shoaling thermocline in the eastern equatorial Indian Ocean in response to greenhouse gas (GHG) increase (Vecchi and Soden 2007; Du and Xie 2008; Zheng et al. 2010). Most often, SST patterns induced by global warming are distinct from natural modes of variability (Xie et al. 2010; DiNezio et al. 2010).

Long hindcasts with realistic eddy-resolving ocean GCMs forced by observed winds show large variability in subduction rate in the central mode water formation region, which is correlated with the Pacific decadal oscillation index (Yamanaka et al. 2008; Qu and Chen 2009). Yamanaka et al. further detect a significant response in STCC in their model hindcast. These results from realistic model hindcasts are suggestive of a STCC mode as examined here based on a free-running coupled GCM. Further studies are needed to clarify physical processes that cause subduction rate to vary, especially with regard to the relative importance of local atmospheric forcing (Hanawa 1987; Qu and Chen 2009) versus modulation of subsurface stratification by Rossby waves (Qiu and Chen 2006).

The eastern STCC is too strong in CM, a bias common to other climate models (not shown). In this and other models, the isopycnal PV minimum of mode water is very sharp and persistent downstream while in observations the PV minimum is much more diffused as it begins its journey southward in the subtropical gyre (Fig. 2 of this paper versus Fig. 9 of Kobashi et al. 2006). Noneddy-resolving models simulate too strong mode water and may exaggerate mode water dynamics, allowing PV anomalies to propagate undissipated (Fig. 10). There is evidence that the low-PV tongue is more diffused in high-resolution ocean GCMs (H. Sasaki et al. 2010), suggestive of mixing effects by mesoscale eddies. One such eddy-resolving model, however, still shows mode water effects on STCC variability (Yamanaka et al. 2008). Subducted temperature–salinity anomalies are observed to circulate in the North Pacific subtropical gyre (Deser et al. 1996; Schneider et al. 1999), a propagation pattern captured by Argo floats that have vastly improved subsurface measurements (Y. N. Sasaki et al. 2010). In light of the dynamical effect and model biases as illustrated here and elsewhere, mode water ventilation, its variability, and coupling with the atmosphere emerge as important topics for ocean circulation and climate research.

Acknowledgments. We thank R. Furue for a helpful discussion on the appendix and anonymous reviewers for helpful comments. This work is supported by the Qianren project, Changjiang Scholar Program, 111 Project (B07036) of the Chinese Ministry of Education, Natural Science Foundation of China (40830106 and 40921004), the U.S. National Science Foundation, National Aeronautic and Space Administration, and the Japan Agency for Marine-Earth Science and Technology. The work was initiated on SPX's sabbatical leave visits to NCAR and GFDL in 2008. He wishes to thank Clara Deser, Gabe Vecchi, Anand Gnanadesikan, and other colleagues there for their hospitality and useful discussions.

APPENDIX

Baroclinic Adjustment to Mode Water Intrusion

Consider a 2.5-layer model in Fig. A1. The total mass transport in the top two layers follows the Sverdrup relationship

$$g_1' z_1^2 + g_2' z_2^2 = g_1' z_{1E}^2 + g_2' z_{2E}^2 + 2\frac{f^2}{\beta}\int_{x_E}^{x} w_e \, dx, \quad \text{(A1)}$$

where g' is the reduced gravity, z is the layer depth, subscripts 1 and 2 denote the upper and lower pycnoclines, subscript E denotes the eastern boundary ($x = x_E$), f and β are the Coriolis parameter and its meridional derivative, and w_e is the Ekman pumping velocity.

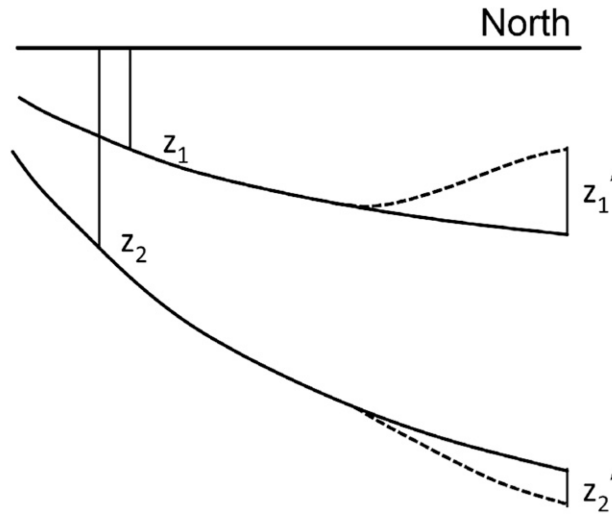

FIG. A1. Schematic of baroclinic adjustment to mode water intrusion. Solid (dashed) curves represent the thermocline before (after) the adjustment.

Now consider an intrusion of mode water, say in response to a deepening of the mixed layer in KOE. This thickens the second layer by h_2' (dashed curves in Fig. A1). Assume that neither eastern boundary stratification nor wind has changed. Linearizing (A1) yields

$$g_1' Z_1 z_1' + g_2' Z_2 z_2' = 0, \quad \text{(A2)}$$

where Z_i denotes the background state, and the prime denotes perturbation. With $z_2' - z_1' = h_2'$, we obtain

$$z_1' = -\frac{g_2' Z_2}{g_1' Z_1 + g_2' Z_2} h_2', \quad \text{and} \quad z_2' = \frac{g_1' Z_1}{g_1' Z_1 + g_2' Z_2} h_2'. \quad \text{(A3)}$$

If $g_1' = g_2'$ and $Z_2 = 2Z_1$, the solution simplifies into $z_1' = -{}^2\!/_3 h_2'$ and $z_2' = {}^1\!/_3 h_2'$.

Thus, the intrusion of mode water shoals the upper pycnocline while deepening the lower pycnocline, an adjustment of the second baroclinic structure in the vertical. The deepened lower pycnocline accelerates the westward flow in the lower layer on the south flank of the mode water, while the poleward shoaling of the upper pycnocline adds an eastward shear to the flow in the upper layer. The latter effect creates the STCC in the model and observations (Fig. 3).

REFERENCES

Alexander, M. A., C. Deser, and M. S. Timlin, 1999: The reemergence of SST anomalies in the North Pacific Ocean. *J. Climate,* **12,** 2419–2433.

Aoki, Y., T. Suga, and K. Hanawa, 2002: Subsurface subtropical fronts of the North Pacific as inherent boundaries in the ventilated thermocline. *J. Phys. Oceanogr.,* **32,** 2299–2311.

Capotondi, A., M. A. Alexander, and C. Deser, 2003: Why are there Rossby wave maxima at 10°S and 13°N in the Pacific? *J. Phys. Oceanogr.,* **33,** 1549–1563.

Ceballos, L. I., E. Di Lorenzo, C. D. Hoyos, N. Schneider, and B. Taguchi, 2009: North Pacific Gyre Oscillation synchronizes climate fluctuations in the eastern and western boundary systems. *J. Climate,* **22,** 5163–5174.

Delworth, T. L., and Coauthors, 2006: GFDL's CM2 global coupled climate models. Part I: Formulation and simulation characteristics. *J. Climate,* **19,** 643–674.

Deser, C., M. A. Alexander, and M. S. Timlin, 1996: Upper ocean thermal variations in the North Pacific during 1970–91. *J. Climate,* **9,** 1840–1855.

——, ——, and ——, 1999: Evidence for a wind-driven intensification of the Kuroshio Current Extension from the 1970s to the 1980s. *J. Climate,* **12,** 1697–1706.

DiNezio, P., A. Clement, and G. A. Vecchi, 2010: Reconciling differing views of tropical Pacific climate change. *Eos, Trans. Amer. Geophys. Union,* **91,** doi:10.1029/2010EO160001.

Du, Y., and S.-P. Xie, 2008: Role of atmospheric adjustments in the tropical Indian Ocean warming during the 20th century in climate models. *Geophys. Res. Lett.,* **35,** L08712, doi:10.1029/2008GL033631.

GFDL Global Atmospheric Model Development Team, 2004: The new GFDL global atmosphere and land model AM2/LM2: Evaluation with prescribed SST simulations. *J. Climate,* **17,** 4641–4673.

Gnanadesikan, A., and Coauthors, 2006: GFDL's CM2 global coupled climate models. Part II: The baseline ocean simulation. *J. Climate,* **19,** 675–697.

Hanawa, K., 1987: Interannual variations of the winter-tie outcrop area of subtropical mode water in the western North Pacific Ocean. *Atmos.–Ocean,* **25,** 358–374.

——, and L. D. Talley, 2001: Mode waters. *Ocean Circulation and Climate,* International Geophysics Series, G. Siedler et al., Eds., Elsevier, 373–386.

Hosoda, S., S.-P. Xie, K. Takeuchi, and M. Nonaka, 2004: Interdecadal temperature variations in the North Pacific central mode water simulated by an OGCM. *J. Oceanogr.,* **60,** 865–877.

Huang, R. X., and B. Qiu, 1994: Three-dimensional structure of the wind-driven circulation in the subtropical North Pacific. *J. Phys. Oceanogr.,* **24,** 1608–1622.

Kobashi, F., H. Mitsudera, and S.-P. Xie, 2006: Three subtropical fronts in the North Pacific: Observational evidence for mode water–induced subsurface frontogensis. *J. Geophys. Res.,* **111,** C09033, doi:10.1029/2006JC003479.

——, S.-P. Xie, N. Iwasaka, and T. Sakamoto, 2008: Deep atmospheric response to the North Pacific oceanic subtropical front in spring. *J. Climate,* **21,** 5960–5975.

Kubokawa, A., 1999: Ventilated thermocline strongly affected by a deep mixed layer: A theory for subtropical countercurrent. *J. Phys. Oceanogr.,* **29,** 1314–1333.

——, and T. Inui, 1999: Subtropical countercurrent in an idealized ocean GCM. *J. Phys. Oceanogr.,* **29,** 1303–1313.

——, and S.-P. Xie, 2002: On steady response of a ventilated thermocline to enhanced Ekman pumping. *J. Oceanogr.,* **58,** 565–575.

Ladd, C., and L. Thompson, 2001: Water mass formation in an isopycnal model of the North Pacific. *J. Phys. Oceanogr.,* **31,** 1517–1537.

——, and ——, 2002: Decadal variability of North Pacific central mode water. *J. Phys. Oceanogr.,* **32,** 2870–2881.

Lee, H.-C., 2009: Impact of atmospheric CO_2 doubling on the North Pacific subtropical mode water. *Geophys. Res. Lett.,* **36,** L06602, doi:10.1029/2008GL037075.

Liu, Q., and H. Hu, 2007: A subsurface pathway for low potential vorticity transport from the central North Pacific toward Taiwan Island. *Geophys. Res. Lett.,* **34,** L12710, doi:10.1029/2007GL029510.

——, and L. Li, 2007: Baroclinic stability of oceanic Rossby wave in the North Pacific subtropical eastward countercurrent. *Chinese J. Geophys.,* **50,** 84–93.

Liu, Z., 1993: Interannual positive feedbacks in a simple extratropical air–sea coupling system. *J. Atmos. Sci.,* **50,** 3022–3028.

——, and M. Alexander, 2007: Atmospheric bridge, oceanic tunnel, and global climatic teleconnections. *Rev. Geophys.,* **45,** RG2005, doi:10.1029/2005RG000172.

Luo, Y., Q. Liu, and L. M. Rothstein, 2009: Simulated response of North Pacific mode waters to global warming. *Geophys. Res. Lett.,* **36,** L23609, doi:10.1029/2009GL040906.

Luyten, J. R., J. Pedlosky, and H. Stommel, 1983: The ventilated thermocline. *J. Phys. Oceanogr.,* **13,** 292–309.

Miller, A. J., D. R. Cayan, and W. White, 1998: A westward-intensified decadal change in the North Pacific thermocline and gyre-scale circulation. *J. Climate,* **11,** 3112–3127.

Nakamura, H., 1996: A pycnostad on the bottom of the ventilated portion in the central subtropical North Pacific: Its distribution and formation. *J. Oceanogr.,* **52,** 171–188.

Nonaka, M., H. Nakamura, Y. Tanimoto, T. Kagimoto, and H. Sasaki, 2006: Decadal variability in the Kuroshio–Oyashio Extension simulated in an eddy-resolving OGCM. *J. Climate,* **19,** 1970–1989.

Oka, E., S. Kouketsu, K. Toyama, K. Uehara, T. Kobayashi, S. Hosoda, and T. Suga, 2011: Formation and subduction of central mode water based on profiling float data, 2003–08. *J. Phys. Oceanogr.,* **41,** 113–129.

Qiu, B., 1999: Seasonal eddy field modulation of the North Pacific Subtropical Countercurrent: TOPEX/Poseidon observations and theory. *J. Phys. Oceanogr.,* **29,** 2471–2468.

——, and S. Chen, 2005: Variability of the Kuroshio Extension jet, recirculation gyre, and mesoscale eddies on decadal timescales. *J. Phys. Oceanogr.,* **35,** 2090–2103.

——, and ——, 2006: Decadal variability in the formation of the North Pacific subtropical mode water: Oceanic versus atmospheric control. *J. Phys. Oceanogr.,* **36,** 1365–1380.

Qu, T., and J. Chen, 2009: A North Pacific decadal variability in subduction rate. *Geophys. Res. Lett.,* **36,** L22602, doi:10.1029/2009GL040914.

——, S.-P. Xie, H. Mitsudera, and A. Ishida, 2002: Subduction of the North Pacific mode waters in a global eddy-resolving GCM. *J. Phys. Oceanogr.,* **32,** 746–763.

Sasaki, H., S.-P. Xie, B. Taguchi, M. Nonaka, and Y. Masumoto, 2010: Seasonal variations of the Hawaiian Lee Countercurrent induced by the meridional migration of the trade winds. *Ocean Dyn.,* **60,** 705–715.

Sasaki, Y. N., N. Schneider, N. Maximenko, and K. Lebedev, 2010: Observational evidence for propagation of decadal spiciness anomalies in the North Pacific. *Geophys. Res. Lett.,* **37,** L07708, doi:10.1029/2010GL042716.

Schneider, N., and A. J. Miller, 2001: Predicting western North Pacific Ocean climate. *J. Climate,* **14,** 3997–4002.

——, ——, M. A. Alexander, and C. Deser, 1999: Subduction of decadal North Pacific temperature anomalies: Observations and dynamics. *J. Phys. Oceanogr.,* **29,** 1056–1070.

Suga, T., K. Hanawa, and Y. Toba, 1989: Subtropical mode water in the 137°E section. *J. Phys. Oceanogr.,* **19,** 1605–1618.

——, Y. Takei, and K. Hanawa, 1997: Thermostad distribution in the North Pacific subtropical gyre: The central mode water and the subtropical mode water. *J. Phys. Oceanogr.,* **27,** 140–152.

Sugimoto, S., and K. Hanawa, 2005: Remote reemergence areas of winter sea surface temperature anomalies in the North Pacific. *Geophys. Res. Lett.,* **32,** L01606, doi:10.1029/2004GL021410.

Taguchi, B., S.-P. Xie, N. Schneider, M. Nonaka, H. Sasaki, and Y. Sasai, 2007: Decadal variability of the Kuroshio Extension: Observations and an eddy-resolving model hindcast. *J. Climate,* **20,** 2357–2377.

Thompson, L., and J. T. Dawe, 2007: Propagation of wind and buoyancy forced density anomalies in the North Pacific: Dependence on ocean model resolution. *Ocean Modell.,* **16,** 277–284.

Tokinaga, H., S.-P. Xie, F. Kobashi, and Y. Tanimoto, 2009: Local and remote influences of the Kuroshio Extension on the atmosphere. *CLIVAR Variations,* No. 7, International CLIVAR Project Office, Southampton, United Kingdom, 1–4.

Uda, M., and K. Hasunuma, 1969: The eastward subtropical countercurrent in the western North Pacific Ocean. *J. Oceanogr. Soc. Japan,* **25,** 201–210.

Vecchi, G. A., and B. J. Soden, 2007: Global warming and the weakening of the tropical circulation. *J. Climate,* **20,** 4316–4340.

Williams, R. G., 1991: The role of the mixed layer in setting the potential vorticity of the main thermocline. *J. Phys. Oceanogr.,* **21,** 1803–1814.

Wittenberg, A. T., A. Rosati, N.-C. Lau, and J. J. Ploshay, 2006: GFDL's CM2 global coupled climate models. Part III: Tropical Pacific climate and ENSO. *J. Climate,* **19,** 698–722.

Xie, S.-P., T. Kunitani, A. Kubokawa, M. Nonaka, and S. Hosoda, 2000: Interdecadal thermocline variability in the North Pacific for 1958–97: A GCM simulation. *J. Phys. Oceanogr.,* **30,** 2798–2813.

——, W. T. Liu, Q. Liu, and M. Nonaka, 2001: Far-reaching effects of the Hawaiian Islands on the Pacific Ocean–atmosphere. *Science,* **292,** 2057–2060.

——, C. Deser, G. A. Vecchi, J. Ma, H. Teng, and A. T. Wittenberg, 2010: Global warming pattern formation: Sea surface temperature and rainfall. *J. Climate,* **23,** 966–986.

Yamanaka, G., H. Ishizaki, M. Hirabara, and I. Ishikawa, 2008: Decadal variability of the subtropical front of the western North Pacific in an eddy-resolving ocean general circulation model. *J. Geophys. Res.,* **113,** C12027, doi:10.1029/2008JC005002.

Yasuda, T., and K. Hanawa, 1997: Decadal changes in the mode waters in the midlatitude North Pacific. *J. Phys. Oceanogr.,* **27,** 858–870.

Yoshida, K., and T. Kidokoro, 1967: A subtropical countercurrent in the North Pacific—An eastward flow near the subtropical convergence. *J. Oceanogr. Soc. Japan,* **23,** 88–91.

Zheng, X.-T., S.-P. Xie, G. A. Vecchi, Q. Liu, and J. Hafner, 2010: Indian Ocean dipole response to global warming: Analysis of ocean–atmospheric feedbacks in a coupled model. *J. Climate,* **23,** 1240–1253.